The laminar-turbulent transition in a fibre laser

E.G. Turitsyna, S.V. Smirnov, S. Sugavanam, N. Tarasov, X. Shu, S.A. Babin, E.V. Podivilov, D.V. Churkin, G. Falkovich, and S. K. Turitsyn

Supplementary Information

Definitions and the laser-fluid analogy

We define "condensate" as a state coherent across the system. We measured coherence by a two-point correlation function, having a finite limit when the distance between points increases up to a system size. In our case of fibre lasers, condensate is the state that appears due to classical wave condensation after spectrally narrow pumping grows coherent radiation out of a spectrally wide initial noise. In fluids, laminar flow is coherent across the system, so also can be considered a condensate. "Onset of turbulence" means (partial) loss of coherence so that, for instance, correlation function decreases with the distance. In a fully turbulent state, the correlation function goes to zero as the distance increases. A system is linearly stable when it is stable with respect to infinitesimally small perturbations.

We explored an analogy here between lasers and fluid, based on the fundamental facts that the coherent state is linearly stable in both systems, and that the transition corresponding to a loss of spatial coherence is probabilistic in nature.

In fluid flows, the dimensionless control parameter is the Reynolds number (Re) which is the ratio of viscous dissipation time and nonlinear (inertial) time, or the ratio of nonlinear and linear terms in the Navier-Stokes equation. Analogously, the ratio of nonlinear and linear terms in the Nonlinear Schrodinger Equation is the ratio of typical dispersion time to the time of nonlinear interaction. It must play the role of the

dimensionless control parameter that governs the laser system[1]. Laminar regime is expected to correspond to lower nonlinearity than turbulence, yet the precise value of the control parameter for turbulence onset in linearly stable systems is sensitive to many properties of the system. For example, using very smooth pipe walls and reducing external noise can keep flow laminar until a very high Re. Similarly, we show below that a low-noise pumping and special mirrors at laser ends are needed for condensate to exist.

Turbulence onset in a pipe increases drag, thus decreasing mean velocity and the effective Reynolds number (velocity times radius divided by viscosity). In our optical system, the dimensionless control parameter R is proportional to the total nonlinearity, γI, and inversely proportional to the total dispersion over the spectrum, $R = \gamma I / \beta_2 \Gamma^2$, where Γ is the spectral width. Fig. S1 shows how the value of the control parameter R, calculated from experimental data, grows with the pump power and then drops at the transition, mainly because the spectral width increases.

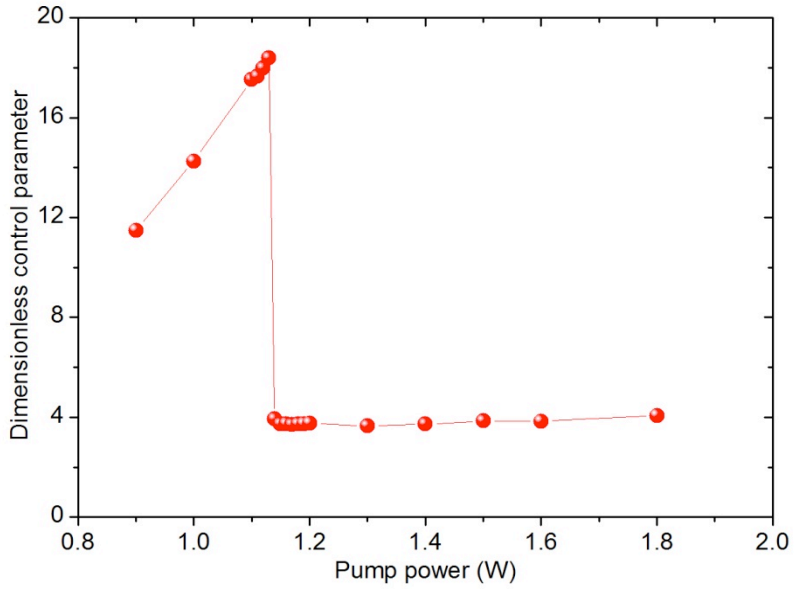

Figure S1. Dimensionless control parameter, $R = \gamma I/\beta_2 \Gamma^2$, versus pump power.

Experimental details

We studied the transition from laminar to turbulent state in a Raman fibre laser, based on high normal-dispersion fibre (Fig. S2). The system was pumped at 1455 nm by semi-CW watt level pump laser, and radiates at a Stokes wavelength near 1550 nm. We used a standard all-fibre design, with a cavity made from high normal-dispersion fibre placed between custom-designed, all-fibre laser mirrors – fibre Bragg gratings. The fibre dispersion and nonlinearity coefficients were $\beta_2=56\ ps^2/km$ and $\gamma=3\ km^{-1}W^{-1}$ (both values were at 1550 nm). The fibre length (L) in our experiments was 770 meters. The mirrors had super-Gaussian spectral profiles of the sixth order, at around 2 nm bandwidth, with dispersion variation less than 10 ps per bandwidth. Spectral and temporal properties of the laser radiation were analysed using a commercial optical-spectrum analyser and an oscilloscope of 36 GHz real-time bandwidth, comparable to the optical bandwidth of the radiation.

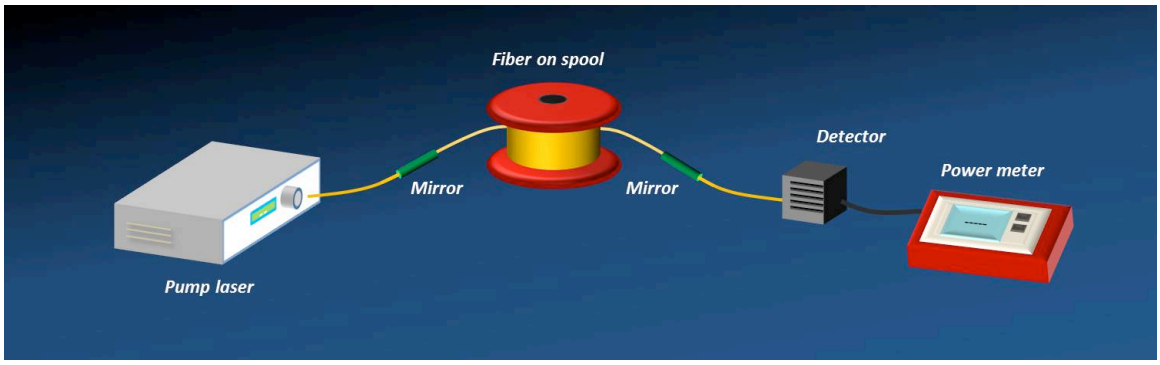

Figure S2. Experimental setup.

We measured how light intensity I depends on the fast time t over a period of time much longer than the laser-cavity round-trip time. Measurements were performed at the fixed point over the longitudinal coordinate. Our time trace could be as long as 6 milliseconds. Having the cavity round-trip time of $\tau_{rt}=2Ln/c = 7.7\ \mu s$ meant that each time series could be up to 800 cavity round trips. Trace was taken at 80Gs/s sampling rate

each time, corresponding to 12.5 ps sampling in the time domain. Measurements were performed within 36 GHz electrical bandwidth. The length of the time trace was limited by the size of the oscilloscope internal memory.

In the intensity plot *I(t)*, a significant increase of fluctuations was visible at the transition point (Fig. S3). Some fluctuations existed, in the laminar regime as well, because of the residual effects of polarization scrambling, pump wave-intensity fluctuation transfer, and influence of laser-mirror dispersion (more details below). Statistical analysis over a number of long-time series resulted in the intensity pdf function (Fig. 1b).

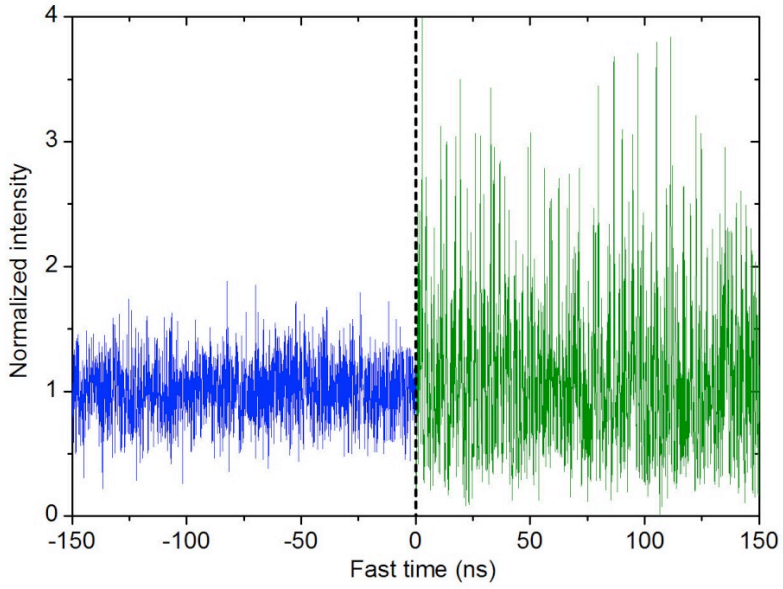

Figure S3. Experimentally measured laser dynamics before (left, blue) and after (right, green) the transition point. Measurements were done at different times. The colour code and powers are the same as in Fig.1. The fluctuations were suppressed in the laminar regime. The probability of large-intensity fluctuations is higher in the turbulent regime.

To plot the spatio-temporal evolution of the intensity $I(t,T)$, we found an exact value of the cavity round-trip time τ_{rt}. We plotted the intensity autocorrelation function $K(\tau) = \langle I(t,T) \times I(t+\tau,T) \rangle$ and measured the time difference between corresponding ACF maxima. Long-time traces $I(t)$ were sliced into segments using τ_{rt}. Each segment had a length equal to round-trip time τ_{rt}. We finally plotted segments one after another, using colour coding for intensity values. We obtained the intensity evolution $I(t,T)$ over fast time t and evolution coordinate T (Fig. 2), which allowed us to analyse spatio-temporal properties of the radiation, including the presence of long-lived structures. Our procedure implies that the resolution over T (in terms of round trips) is always one round-trip.

To establish the laminar regime, the main factors were low noise levels in the system and special laser mirrors. Additional noise in the pump wave makes generation turbulent at all powers. Intensity fluctuations in the pump wave are transferred through cross-phase modulation (XPM) to the generation of Stokes wave that leads to stochastisation and spectral broadening of the generation wave[2]. Such a transfer was observed in the radio-frequency spectrum[3]. We minimized the influence of pump-to-Stokes noise transfer by using the special pump laser, which suppressed relative intensity noise down to -120 dB/Hz.

Polarization scrambling could also destroy the laminar regime. We used two polarization controllers inside the cavity to manage polarization of the generated radiation and achieve the laminar regime. We used independent polarization measurements to control the state of polarization during measurements. Residual scrambling still existed, as we had a degree of polarization value only up to 0.9, and DOP could be lower at frequencies above our polarization measurement bandwidth (250 MHz). This could be a source of noise measured in the experiment.

We used custom-designed, dispersion-free, ultra-wideband, super-Gaussian shaped laser mirrors to realize laminar-turbulent transition. The laser-mirror dispersion was crucial for observing the transition. Using mirrors with standard (nonoptimized, nonzero) dispersion profiles, only turbulent stochastic generation was observed both in the numerical modelling and in the experiment. In this case, the condensate was destroyed by the phase randomization of the modes after each round-trip reflection from the mirrors. We used mirrors with super-Gaussian spectral profiles of the sixth order, with a dispersion variation less than 10 ps per 2 nm bandwidth. This was crucial for the experimental realization of transition. Mirrors were written by an on-site Bragg gratings writing facility directly in a fibre core, following the longitudinal profile of the refractive index, which was numerically calculated to obtain desired spectral and dispersion response.

Finally, the spectral shape of the laser mirrors is also critically important to realize the laminar generation. There is an energy flux from the condensate to the spectral wings. The wings are filtered out from the cavity at each reflection from the mirror. When mirrors were spectrally narrow or had smooth, bell-shaped spectral profiles, this resulted in more energy losses, so more energy was needed from the condensate to recover the spectral wings at the next round trip. To achieve condensate generation over many round trips, we used the specially designed and fabricated laser mirrors of rectangular wide-band spectral profiles. Fig. S4 shows remarkable dependence of the radiation linewidth on the mirror spectral width in two lasers, having the laser mirrors of conventional dispersion of ~1000 ps/nm (Fig. S4, blue circles) and dispersion-optimized laser mirrors (Fig. S4, red circles). For the laser system with conventional laser mirrors, the generation is always turbulent. The spectral width and, consequently, the number of generated modes increased monotonically with the mirror spectral width (Fig. S4, blue circles), as

expected for a usual laser[4]. For a laser system with dispersion-optimized mirrors, the radiation spectral width is comparable to the mirror spectral width and grows only up to 1.5 nm of the mirror spectral width. The generation was turbulent in this case. Contrary to expectations, the radiation spectral width decreased with increasing mirror spectral width, and eventually saturated at low value (Fig. S4, red circles), when the laminar generation was established. There were no losses, and the radiation did not change its spectral shape during a round trip for a very wide spectral profile of the mirror. For narrower spectral profiles of the mirror, the losses on spectral wings upon reflection must be compensated by pumping during the round trip, which leads to spectral broadening.

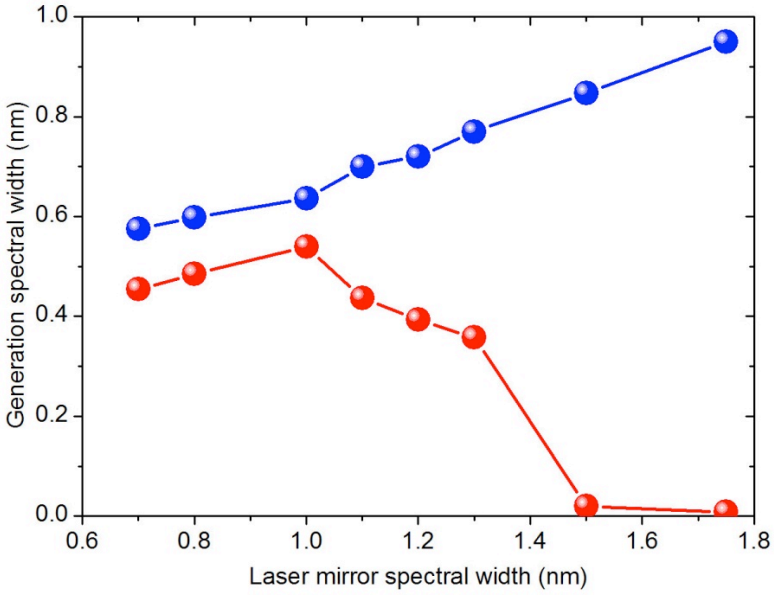

Figure S4. Numerically calculated spectral width of generated radiation as a function of the laser mirror spectral width for identical fibre-laser systems, differing only by the laser mirror dispersion. Blue circles correspond to the case when the laser mirrors had sufficient dispersion, and the laser only generated in a turbulent regime. Red circles correspond to the case when the laser mirrors were dispersion-optimized, so the laminar generation was feasible at large spectral width of mirrors.

Numerical modelling

Numerical modelling was based on two complementary approaches: Analysis of longitudinal resonator modes evolution with round trips; and computation of field dynamics using generalized NSEs.

Analysis of longitudinal resonator modes was based on the well-established mathematical model that presents the standard, slow round-trip evolution equation for the longitudinal $E_m = \int E(t)e^{-i\Omega_m t}dt$ modes of the envelope. This can be derived from the generalized Schrödinger equations for backward and forward Stokes waves:

$$\frac{\tau_{RT}}{L}\frac{dE_m}{dT} = \left(G_m - i\beta_2\Omega_m^2\right)E_m - i\gamma\sum_{i,k}E_iE_kE_{i+k-m}^*$$

Here, $\tau_{rt}= 2Ln/c$ is the round-trip time (n is the refractive group index), L is the resonator length, and c is the speed of light in vacuum. The terms on the right-hand side describe respectively gain/loss (G_m), group-velocity dispersion (β_2) and the four-wave nonlinear interaction (including cross-phase and self-phase modulation) induced by the Kerr nonlinearity. This equation has the simplest stationary solution in the form of an ideal one-mode (or a pair of modes) condensate that corresponds to the maximum of (G_m). Such a monochromatic wave is linearly unstable in the case of ($\beta_2<0$) (the so-called modulation instability) and is linearly stable in the case of ($\beta_2>0$). In this work, we considered the case of normal ($\beta_2>0$) dispersion.

In the simplest scheme, we only treated the integral pumping intensity (the part of the gain/loss G_m) as a function of T. For more detailed comparison with the experiment and better resolution of the details of t-dependence, we used a more sophisticated model, which was the coupled set of NSEs for the radiation and the pumping wave amplitudes as functions of both T and t.

$$\frac{\partial E_p^{\pm}}{\partial z}+\left(\frac{1}{v_s}-\frac{1}{v_p}\right)\frac{\partial E_p^{\pm}}{\partial t}+\frac{i}{2}\beta_{2p}\frac{\partial^2 E_p^{\pm}}{\partial t^2}+\frac{\alpha_p}{2}E_p^{\pm}=i\gamma_p\left|E_p^{\pm}\right|^2 E_p^{\pm}-\frac{g_p}{2}\left(\left\langle\left|E_s^{\pm}\right|^2\right\rangle+\left\langle\left|E_s^{\mathrm{m}}\right|^2\right\rangle\right)E_p^{\pm}$$

$$\frac{\partial E_s^{\pm}}{\partial z}+\frac{i}{2}\beta_{2s}\frac{\partial^2 E_s^{\pm}}{\partial t^2}+\frac{\alpha_s}{2}E_s^{\pm}=i\gamma_s\left|E_s^{\pm}\right|^2 E_s^{\pm}+\frac{g_s}{2}\left(\left\langle\left|E_p^{\pm}\right|^2\right\rangle+\left\langle\left|E_p^{\mathrm{m}}\right|^2\right\rangle\right)E_s^{\pm}$$

Here, t stands for time in the frame of references moving with the pump wave, $v_s v_p$ are pump and Stokes waves group-velocities, ± denotes counter-propagating waves, and z is the longitudinal coordinate. Evolution coordinate T is related with longitudinal coordinate z by following relation $T=\frac{z}{2L}\tau_{RT}$. The number of round trips is $N=\frac{z}{2L}$. The values of s and p are used for Stokes and pump waves. At generation power levels less than 1 W, the typical nonlinear length L_{NL} is around 1 km, which is much longer than walk-off length L_w ~*1* m, related with difference of pump and Stokes-waves group velocities v_p, v_s. Equations were averaged over length L_a, being $L_w<<L_a<<L_{NL}$. We used a relatively small number of the spectral components within spectral window (usually 2^{14}) as it is impossible to use the real number of modes (up to 10^6 in turbulent regime). So the width of temporal window in which the complex field *E(t)* is calculated is much shorter than the cavity round trip time. Boundary conditions over the temporal window are assumed to be periodic. We checked that our results do not depend on the number of longitudinal modes used in calculations in the range 2^{12}-2^{16}. We omitted the XPM term between pump and Stokes waves. The more sophisticated model took into account the fluctuation of the gain because of the fluctuations in the highly multi-mode, partially coherent, turbulent pump wave. The values of the coefficients used in numerical modelling were: α_p = 0.07 *dB/km*, α_s = 0.052 *dB/km*, β_{2p} = 34 ps^2/km (normal), β_{2s}=56 ps^2/km (normal), γ_s =3 $(km*W)^{-1}$, g_s =*0.6* $(km*W)^{-1}$. The cavity length was normally 770 m (as in experiments), but we also checked the generality of the results by varying the cavity length (for example, 370 m in Figs. 2c–d, up to 13 km in Fig. 3). We observed

similar results on transition to turbulent regimes for all systems we considered. Moreover, the results of the two different numerical models agreed. The only difference was that the second model demonstrated a slightly higher level of fluctuation in the laminar phase.

In addition to the power, spectral properties and intensity evolution of the radiation, we can calculate properties in numerical modelling, which are still impossible to measure. The main limitation of the experiment is that it only measured intensity values, whereas all the phase information was lost. In numerical modelling, both intensity and phase information are available, which allows for calculating the dispersion relation. To do this, we computed and stored the complex field $E(t)$ (time dynamics) and its discrete Fourier transform $E(\omega)$ (optical spectrum) at the beginning of each round trip. The first round trip gave us the values $E(t,z=0)$ and $E(\omega,z=0)$. The second round trip gave $E(t,z=2L)$ and $E(\omega,z=2L)$. L is the cavity length. We repeated the procedure for 1,024 successive round trips, resulting in the discrete (over both ω and z) function $E(\omega,z)$. After a discrete Fourier transform over z, we got $E(\omega,k)$ function. Its square modulus $I(\omega,k)$ is shown in Fig S5 as a colour contour plot.

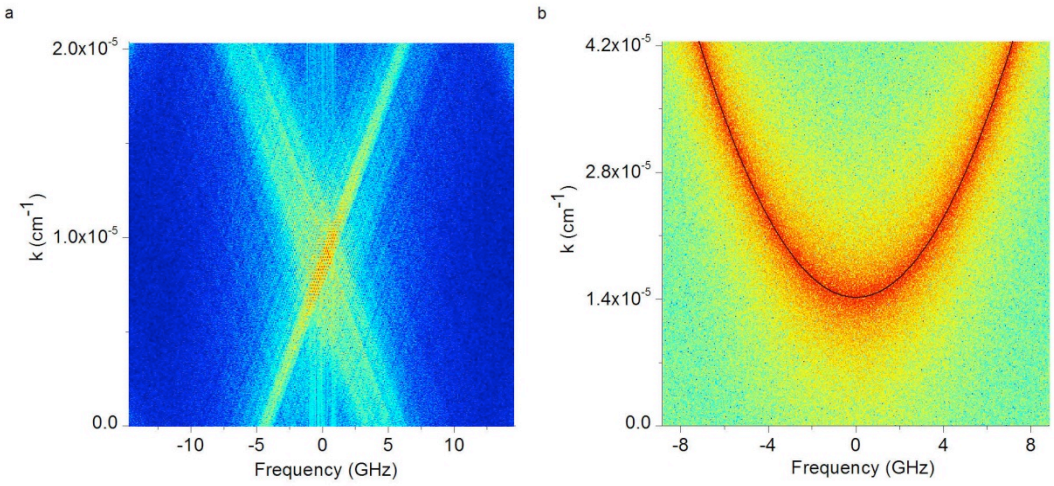

Figure S5. Numerically calculated dispersion relations in a) laminar and b) turbulent regimes. The colour code displays intensity in logarithmic scale. The black solid curve is a parabolic eye guide.

In addition, numerical modelling allowed us to resolve the internal temporal shape of the coherent structures, which could not be experimentally measured because of limited real-time resolution. Fig. S6 is devoted to identifying the coherent structures that proliferate before the transition. A typical coherent structure is shown in Fig. S6a to have a specific dark-soliton *tanh(t)* shape[5]. The phase shift on a soliton is directly related to the soliton amplitude and is exactly π for a dark soliton. Grey solitons have continuous phase across the structure, which is clearly visualized on the phase portrait (Fig. S6b). Non-interacting solitons should looks like a chord on the phase portrait. The deeper the soliton, the closer to the ring centre the chord should be, so the lines inside the ring demonstrate the phase change, or the topological nature of the objects. Bended lines are attributed to interacting solitons. The width of the ring is an amount of the condensate amplitude fluctuations. Fig. S6 proves that the coherent structures that appeared on the condensate in a fibre laser were dark and grey solitons. Numerous such solitons are seen running in Fig. S7 (a view from the bottom i.e. from the zero-intensity level). In particular, the figure clearly shows

the condensate and the initial stage of occurrence of dark and grey solitons that stably propagate and cross each other without visible destruction.

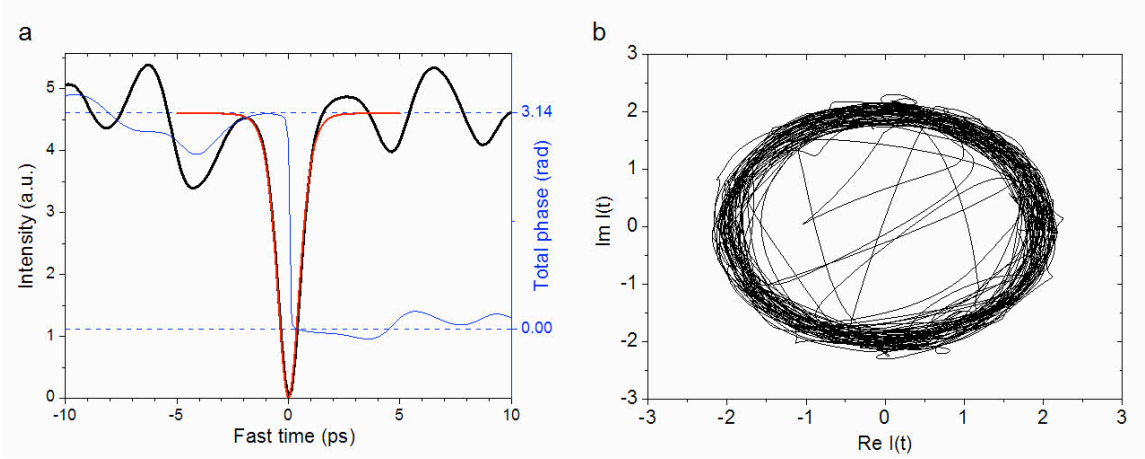

Figure S6. Dark and grey solitons in the laminar regime. a) The intensity dynamics *I(t)* taken from numerical simulations (black) in the laminar regime shown with large zoom over fast time *t*. Analytical shape of a dark soliton (red) fits well with the temporal shape of the coherent structure. The total phase (blue) exhibits π-shift over the dark soliton, in accordance with dark-soliton analytical properties. b) Phase diagram illustrating dark- and grey-soliton phase shifts.

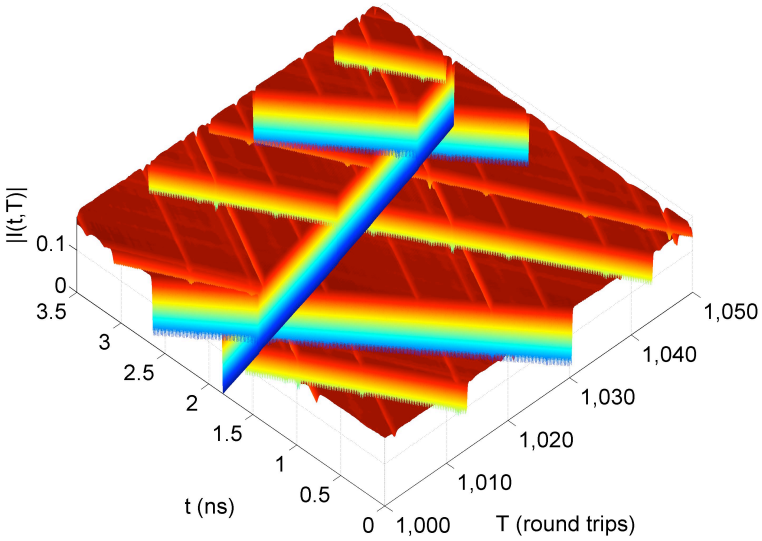

Figure S7. Solitons running over the condensate. One dark standing soliton and several grey solitons are seen running in both directions.

Video S1 is a movie that shows how the intensity evolves over frequency, time and coordinate, in order to visualize the emergence of dark and grey soliton clusters in all their complexity and highlight their key role in laminar-regime destruction. The upper panel shows the evolution of the spectral intensity $I(\omega,t)$ with the Fourier transform calculated by a short-time Fourier transform, with t-interval divided over short 256 windows. The lower panel shows the evolution of $I(t)$. One can see solitons appear, proliferate and then cluster, creating a minimum (running to the right in this case) that eventually splits the condensate and leads to turbulence. Movie also suggests that recurrent interaction of the solitons (due to the roundtrip nature of the experiment reflected by periodic boundary conditions in numerics) may play an important role in the transition; we thank the anonymous referee for this observation. In this respect, our system may be more similar to a cylindrical Taylor-Couette rather than pipe flow. The detailed analysis of the evolution of spectral patterns accompanying soliton clustering will be published elsewhere.

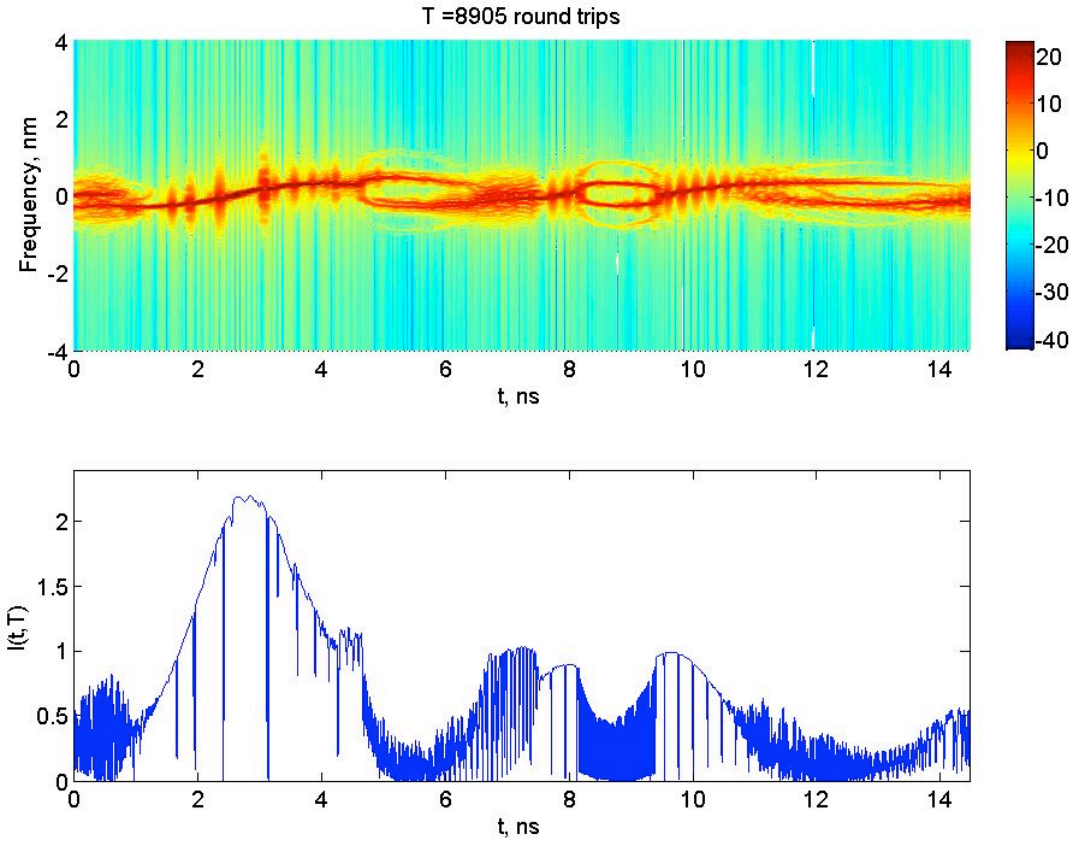

Video S1. Condensate destruction through clustering of dark and grey solitons. Upper panel – the radiation spectrogram showing the local frequency spectrum of the part of the radiation within a 2.3 ns temporal window, after completing 8,906 round trips within the laser cavity. Lower panel – intensity dynamics *I(t)*. The video is provided in a separate file.

After the condensate destruction, some order survived in the system in the form of quasi-periodicity, as can be seen in Fig. S8, showing the dependence of the intensity correlation function on the shift in *T*.

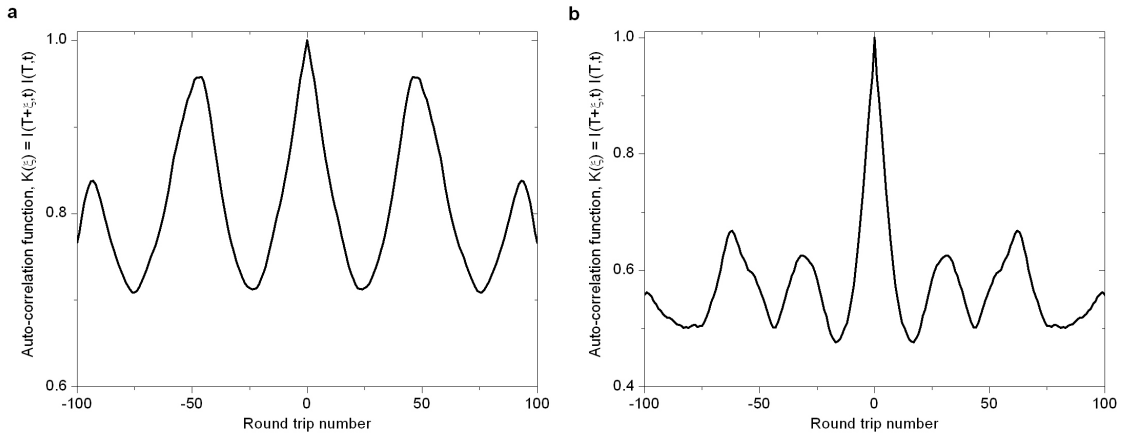

Figure S8. Intensity autocorrelation function over evolution coordinate. a) Experimental. b) Numerical simulations.

References

1. Turitsyna, E. G., Falkovich, G. E., Mezentsev, V. K. & Turitsyn, S. K. Optical turbulence and spectral condensate in long-fiber lasers. *Phys. Rev. A* **80**, 031804(R) (2009).
2. Babin, S. A., Churkin, D. V., Ismagulov, A. E., et al. FWM-induced turbulent spectral broadening in a long Raman fibre laser. *J. Opt. Soc. Am. B* **24**, 1729–1738 (2007).
3. Babin, S. A., Churkin, D. V., Fotiadi, A. A., et al. Relative intensity noise in cascaded Raman fiber lasers. *IEEE Photon. Techn. Lett*. **17**, 2553–2555 (2005).
4. Siegman, A. E. *Lasers* (University Science Books, 1986)
5. Kivshar, Y. S. & Luther-Davies, B. Optical dark solitons: Physics and applications. *Physics Reports* **298,** 81–197 (1998).